

1 Estimating EEG source dipole orientation based on singular-value decomposition for
2 connectivity analysis

3 M. Rubega¹, M. Carboni^{1,2}, M. Seeber¹, D. Pascucci³, S. Tourbier⁴, G. Toscano^{2,5}, P. Van Mierlo^{2,6}, P. Hagmann⁴, G.
4 Plomp³, S. Vulliemoz², C. M. Michel^{1,7}

5 ¹ Functional Brain Mapping Lab, Department of Fundamental Neurosciences, University of Geneva, Geneva, Switzerland

6 ² EEG and Epilepsy Unit, University Hospital of Geneva, Geneva, Switzerland

7 ³ Perceptual Networks Group, Department of Psychology, University of Fribourg, Fribourg, Switzerland

8 ⁴ Department of Radiology, University Hospital of Lausanne, Lausanne, Switzerland

9 ⁵ Unit of sleep medicine and Epilepsy, C. Mondino National Neurological Institute, Pavia, Italy

10 ⁶ Medical Image and Signal Processing Group, Department of Electronics and Information Systems, Ghent University, Ghent, Belgium

11 ⁷ Lemanic Biomedical Imaging Centre (CIBM), Lausanne and Geneva, Switzerland

12

13 Corresponding author: M. Rubega

14 Functional Brain Mapping Lab

15 Campus Biotech

16 Chemin des Mines 9

17 1202 Genève

18 Switzerland

19

20 tel +41 0223790865

21 mail maria.rubega@unige.ch

22

23 ABSTRACT

24 In the last decade, the use of high-density electrode arrays for EEG recordings combined with the
25 improvements of source reconstruction algorithms has allowed the investigation of brain networks dynamics at
26 a sub-second scale. One powerful tool for investigating large-scale functional brain networks with EEG is time-
27 varying effective connectivity applied to source signals obtained from electric source imaging. Due to
28 computational and interpretation limitations, the brain is usually parcelled into a limited number of regions of
29 interests (ROIs) before computing EEG connectivity. One specific need and still open problem is how to represent
30 the time- and frequency-content carried by hundreds of dipoles with diverging orientation in each ROI with one
31 unique representative time-series. The main aim of this paper is to provide a method to compute a signal that

32 explains most of the variability of the data contained in each ROI before computing, for instance, time-varying
33 connectivity. As the representative time-series for a ROI, we propose to use the first singular vector computed by
34 a singular-value decomposition of all dipoles belonging to the same ROI. We applied this method to two real
35 datasets (visual evoked potentials and epileptic spikes) and evaluated the time-course and the frequency content
36 of the obtained signals. For each ROI, both the time-course and the frequency content of the proposed method
37 reflected the expected time-course and the scalp-EEG frequency content, representing most of the variability of
38 the sources (~80%) and improving connectivity results in comparison to other procedures used so far. We also
39 confirm these results in a simulated dataset with a known ground truth.

40 *Keywords.* EEG, source space activity, dipole orientation, visual evoked potentials, epilepsy

41

42 INTRODUCTION

43 Electroencephalography (EEG) records the dynamic of brain networks on a sub-second time scale. The high
44 temporal resolution of EEG allows to study how brain activity propagates and interacts in large-scale networks by
45 applying connectivity measures to the recorded signals. However, connectivity measures based on scalp electrode
46 measurements (sensors space) are not revealing the true interactions among brain sources. Neighbouring
47 electrodes measure signals that are highly correlated, leading connectivity algorithms to estimate sham links.
48 Indeed, the measurements of the voltage potential at various locations on the scalp are the result of the
49 simultaneous activity of many different configurations of distributed current generators in the brain [1] [2] [3] [4].
50 To obtain physiologically plausible results, the reconstruction of brain source activity before computing
51 connectivity is strictly required. Indeed, the distribution of the simultaneously active sources at each moment in
52 time can be localized from the high-density EEG scalp potentials by state-of-the-art distributed source localization
53 algorithms informed by the individual anatomy derived from magnetic resonance imaging (MRI) and realistic
54 volume conduction physics [5] [6] [7] [8] [9]. The estimated activity at each solution point in the brain is described
55 by a three dimensional dipole (x,y,z) . The ill-posed inverse problem can be solved merely by introducing a priori
56 assumptions about the sources and the volume conductor [6]. For instance, LAURA (Local AUtoRegressive
57 Average), one of the distributed linear inverse solutions, imposes additional biophysical and physiological
58 constraints in the minimum norm algorithm [10]. After the estimation of the dipole activity at each solution point,
59 the brain is usually parceled into regions before connectivity estimation, because the full spatial size of the data
60 (more than 5000 solution points) is unreasonable in terms of computations and statistical power. The choice of
61 the parcellation scheme and resolution is crucial as it has effects on network topological characteristics and can
62 be based either on anatomical or functional assumptions [11]. In any case, the optimal choice depends on the
63 type, quality and resolution of data and on the study purpose. The most commonly used anatomical-based
64 parcellation atlases are, among others, the Automated Anatomical Labeling (AAL) atlas [12] [13] and FreeSurfer's
65 Desikan Killiany atlas [14] [15]. After parcellation, it is possible to build a graph representation of the brain [16]
66 where nodes are associated to the brain regions of interest (ROIs), and edge weights are given by functional [17]
67 [18] [19] or effective [20] [21] connectivity measures that are robust to volume conduction effects. To estimate

68 either directed or undirected connectivity, all the solution points estimated in each ROI should be summed up in
69 a unique time-series. The approaches proposed in the literature usually consist of two steps. In the first step, for
70 each dipole, either the norm is computed or the direction of the dipoles is fixed using different techniques. One
71 approach is the computation of the norm (i.e. computing absolute dipole amplitude while discarding the
72 orientation of the dipoles) or the power modulation using the Hilbert transform [22] [23]. This, however, may be
73 problematic for connectivity estimation because the phase information contained in the original signal is lost [24].
74 Other current methods to fix the dipole orientation within a ROI are either the projection to the refined average
75 direction across time and epochs [25]; the selection of the dipole orientation orthogonal to the segmented grey
76 matter based on the assumption that the orientation of the dipoles should resemble the orientation of the apical
77 dendrites of the pyramidal neurons [26] or the selection of the orientation maximizing the projected power [27].
78 The second step consists in either averaging all dipole time-series within the ROI once the dipole orientation is
79 fixed [28] or applying principal component analysis (PCA) to obtain the representative time-series [29] [30].

80 Other popular one-step solutions are either to compute the average cortical activity in each ROI by means of
81 the instantaneous average of the signed magnitude of all the dipoles within the ROI [31] or to consider only the
82 source activity of the solution point closest to the geometric center of each ROI, i.e., the centroid, as the
83 representative source waveform [32] [33] [34] [35]. However, the selection of only one dipole out of hundreds
84 does not necessarily properly represent the activity in a given ROI. Concerning the averaging approach, a common
85 observation is a drastic amplitude reduction. Indeed, due to the extensive folding of the human cerebral cortex,
86 some sources in the ROI may be almost perfectly parallel to each other, but inverted in orientation, leading to
87 cancelation when averaging them. The resulting signal amplitude reduction could lead to decrease in accuracy of
88 the subsequent analysis and affect the final results. For instance, connectivity estimation involves computing the
89 inverse of the matrix containing the representative source waveforms, which, if the values are small, may lead to
90 a bad-conditioned matrix with a high condition number [36], i.e., even a small error in the data can produce a
91 large deviation in the solution. Moreover, low-amplitude time-series may increase the rate of false positive
92 connections, e.g., low-amplitude time-series may easily fit in large-amplitude time-series leading to misleading
93 high autoregressive coefficients [37].

94 In this work, we propose to extract the dominant signal reflecting the main pattern of variation of all the
95 solution points in the same ROI by using Singular-Value Decomposition (SVD) and considering the first singular
96 vector. This method enables both to identify the main direction of all the dipoles of a ROI and to discard the
97 contribution of the outlier dipoles. The novelty with respect to the other approaches proposed in the literature is
98 that SVD provides a *population* signal that incorporates the behavior of all the dipoles within the ROI without
99 choosing or selecting specific active voxels, as it is usually done [38] [29] [30] [27].

100 As a demonstration of the validity of the method, we present the analysis of two different data sets (visual
101 evoked potentials and epileptic spikes) using this method and comparing it to the common procedure of both
102 extracting the time-series of the centroid in each ROI and extracting the time-series with the highest power in
103 each ROI. We also evaluated its performance in realistically simulated data, where the ground-truth is known.

104 METHODS

105 *Data description*

106 *Dataset 1. Visual evoked potential of face perception.* Many behavioral studies have investigated the process
107 involved in visual stimuli such as face images [39] [40] [41]. Traditional measures are based on the N170 face-
108 sensitive evoked response component [42]. Human faces evoke a large negative potential (N170) over the
109 occipital-parietal scalp, more prominent over the right than the left hemisphere, which is reduced in evoked
110 potentials elicited by other animate and inanimate non-face stimuli [43]. Applying effective connectivity in face
111 perception, i.e., describing the network of directional effects of one brain region over another, may be a powerful
112 instrument to study this visual process. In order to study these causal effects, it is important to precisely
113 reconstruct the face-response stimulus in the source space. For this reason, we investigated the ability of our
114 method to reconstruct the dynamics of visual evoked potential (VEP) in source space based on high density EEG
115 (hdEEG) data.

116 Participants (N=13, 2 males, age=24.15 ± 3.41) sat in a dimly lit sound-attenuated and electrically shielded
117 room with their head positioned on a chinrest at ~70 cm from the monitor. Each trial lasted 1.2 seconds and
118 started with a blank screen lasting 500 ms. After the blank interval, one image (either a face or a scramble image)
119 was presented for 200 ms and participants had the remaining 1000 ms to respond. The task was to report whether
120 they saw a face or not (Yes/No task) by pressing two buttons in a response box. Faces and scrambled images were
121 randomly interleaved across trials. After the participant's response, there was a random interval (from 600 to 900
122 ms) before the beginning of a new trial.

123 The experiment consisted of 4 blocks of 150 trials each, for a total of 600 trials, i.e., 300 with faces and 300
124 with scrambled images [44]. For this study, we used the EEG data in response of the face images (300 trials per
125 subject).

126 During the experiment, EEG data were recorded continuously at 1024 Hz through a 128-channel Biosemi
127 Active Two EEG system (Biosemi, Amsterdam, The Netherlands). Electrode impedance was kept < 20 kΩ.

128 *Dataset 2. Interictal epileptiform discharges in focal epilepsy.* hdEEG source imaging plays a central role in
129 diagnosis and management of patients with focal epilepsy [45]. However, recent work in the literature provided
130 evidence that epilepsy is a disorder affecting neural networks [46]. Thus, connectivity measures and graph analysis
131 are promising tools to extract network information from both hdEEG and neuroimaging data [47] [48] [49]. We
132 applied our method on pre-surgical interictal spikes (IEDs) recorded in patients with pharmaco-resistant focal
133 epilepsy, who subsequently underwent epilepsy surgery.

134 The patients (N=7, 3 males, age=23±14 y) were selected from those admitted for pre-surgical evaluation to
135 the EEG & Epilepsy Unit, Department of Clinical Neurosciences, University Hospital of Geneva (HUG), Switzerland.
136 They underwent hdEEG long-term (>4 h) recording with 256 electrodes in the context of their pre-surgical
137 evaluation, and subsequently underwent resection of the estimated epileptogenic zone causing their focal
138 epilepsy. The outcomes of the surgery after 12 months along with the exact location of the resection zone were

139 available from postoperative structural MRI and were used as validation for the localization of the generators of
140 the interictal epileptic discharges.

141 The hdEEG was recorded with the Geodesic Sensor Net with 256 electrodes (Electrical Geodesic, Inc., Eugene,
142 OR, U.S.A.). Electrode-skin impedances were maintained $<15\text{ k}\Omega$. The recordings were sampled at 1 kHz,
143 referenced to Cz. Then, an epileptologist, G.T., marked 41 ± 18 hdEEG epochs containing the interictal spikes for
144 each patient. Then, the 1-s hdEEG epochs centered on the spike peak were used as input of the analysis.

145 *Preprocessing*

146 The VEP EEG signals were downsampled at $f_s = 200\text{ Hz}$ and detrended to remove slow fluctuations and
147 linear trends [50]. The line and monitor noise (50 and 75 Hz, plus harmonics) were attenuated with an adaptive
148 multitaper filter (Cleanline plugin for EEGLAB). EEG epochs were then extracted from the continuous dataset and
149 time-locked from -1000 ms to 1000 ms relative to the onset of each image. Noisy channels were identified by
150 visual inspection and removed before preprocessing. Individual epochs containing non-stereotyped artifacts, peri-
151 stimulus eye blinks and eye movements (occurring within $\pm 500\text{ ms}$ from stimulus onset) were also identified by
152 visual inspection and removed from further analysis (mean number of epochs removed across participants: 6 ± 5).
153 Data were cleaned from remaining physiological artifacts (eye blinks, horizontal and vertical eye movements,
154 muscle potentials and other artifacts) through a PCA-informed ICA algorithm implemented in EEGLAB. After ICA
155 cleaning, the identified artifact channels were interpolated using the nearest-neighbor spline method and the
156 data were re-referenced to the average reference.

157 The EEG data containing the spikes of epileptic patients were filtered from $[0.5\ 40]\text{ Hz}$ with 5th order
158 Butterworth filter avoiding phase distortion. Finally, the data were down-sampled at $f_s = 250\text{ Hz}$.

159 *EEG source estimation*

160 In this study, we applied the LAURA algorithm implemented in Cartool [51] to compute the source
161 reconstruction in the individual MRI applying the Local Spherical Model with Anatomical Constraints (LSMAC) and
162 taking into account the patient's age to calibrate the skull conductivity [10] [52] [53]. The LSMAC method restricts
163 the solution space to the gray matter of the individual brain.

164 *Whole brain segmentation and parcellation*

165 Starting from the high-resolution T1-weighted image, using the Connectome Mapper open-source processing
166 [54] that calls the version 6 of the Freesurfer image analysis suite [55], we resampled the image to isotropic
167 $1\text{ mm}\times 1\text{ mm}\times 1\text{ mm}^3$ and we segmented the whole brain in white matter, grey matter, i.e., cortical and sub-cortical
168 structures, and cerebrospinal fluid based on the anatomical Desikan-Killiany [14] and Destrieux [56] atlases. At
169 the end of the process, the cortex was parcellated into a total of 83 regions, which accounted for all the cortical
170 structures of the Desikan-Killiany anatomical atlas, as well as the deep-grey nuclei and the brainstem [54].

171 *Projection method based on SVD*

172 An estimate of the $x - y - z$ space coordinates of the circa $M = 5000$ cortical dipoles was obtained for
173 each time point. The estimation of the dipole sources $\tilde{\mathbf{x}}$ is based on the solution of the following regularized

174 equation:

$$175 \quad \tilde{\mathbf{x}} = \underset{\mathbf{x}}{\operatorname{argmin}} (\|\mathbf{L}\mathbf{x} - \mathbf{y}\|_N^2 + \gamma^2 \|\mathbf{x}\|_M^2) \quad (1)$$

176 where $\|\cdot\|_M$ represents the M-norm, \mathbf{L} is the lead field matrix, \mathbf{x} the dipole sources, \mathbf{y} the EEG scalp potentials
177 and γ is the regularization parameter which can be estimated by different criteria, e.g., by the L-curve approach
178 [57].

179 Subsequently, first, we associated the dipoles to their respective ROI based on the 82 atlas labels (the
180 brainstem was excluded). Second, for each ROI separately, we collected all the N time samples of the $x - y -$
181 $z -$ space coordinates of the n dipoles included in a given ROI and we organized the data in a matrix
182 \mathbf{D} , $[N \times (n \times 3)]$, as follows:

$$183 \quad \mathbf{D} = \begin{bmatrix} d_{x_1}(t_1) & d_{y_1}(t_1) & d_{z_1}(t_1) & \cdots & d_{x_n}(t_1) & d_{y_n}(t_1) & d_{z_n}(t_1) \\ & \vdots & & \ddots & & \vdots & \\ d_{x_1}(t_N) & d_{y_1}(t_N) & d_{z_1}(t_N) & \cdots & d_{x_n}(t_N) & d_{y_n}(t_N) & d_{z_n}(t_N) \end{bmatrix} \quad (2)$$

184 After that we applied the SVD to this matrix:

$$185 \quad \mathbf{D} = \mathbf{U}\mathbf{S}\mathbf{V}^T \quad (3)$$

186 where the apex T stands for the transpose and the columns of \mathbf{D} can be seen as the linear combinations of
187 the columns of \mathbf{U} with the coefficients given by the columns of $\mathbf{S}\mathbf{V}^T$. Because of the singular values contained in
188 the diagonal of \mathbf{S} appear in a decreasing order, we considered the first column of \mathbf{U} $\mathbf{u}_1 [N \times 1]$, i.e., the
189 orthonormal vector projected along the axis that represents the major orientation of all the dipoles, like the signal
190 that explains most the variability of the data and as the best representation of the ROI content. In other words,
191 Equation (3) assumes that the data matrix \mathbf{D} comprises hidden components \mathbf{u}_i that are mixed together through
192 coefficients \mathbf{S} . Standard matrix factorizations in linear algebra, such as SVD, owe their uniqueness to hard and
193 restrictive constraints such as orthogonality [58].

194 *Connectivity estimation*

195 Among the different techniques for extracting effective connectivity, information partial directed coherence
196 (*iPDC*) properly accounts for size effects in gauging connection strength, as reported in detail in [59]. In
197 particular, *iPDC* is a multivariate spectral measure to compute only the directed influences between any given
198 pair of signals (i, j) of a multivariate dataset. This information is condensed in a complex function $iPDC_{i \leftarrow j}(f)$ of
199 the frequency f , which measures the relative interaction of the signal j with regard to signal i as compared to all
200 j 's interactions to other signals in the multivariate dataset. While we refer the reader to [60] for the mathematical
201 details, the procedure for computing *iPDC* is briefly described by the following two steps.

202 In the first step, the cortical waveforms $\tilde{\mathbf{x}}$ computed after applying the projection method described in the
203 previous section, are fitted against a *time-variant* (tv) multivariate autoregressive (MVAR) model to overcome the
204 problem of non-stationarity of the EEG data. If the EEG data are available as several trials of the same length, the
205 cortical waveforms computed from the EEG data generates a collection of realizations of a multivariate stochastic
206 process which can be combined in a multivariate, multi-trial time series:

$$\tilde{\mathbf{X}}(t) = \begin{bmatrix} \tilde{\mathbf{x}}_1^{(1)}(t) & \cdots & \tilde{\mathbf{x}}_d^{(1)}(t) \\ \vdots & \ddots & \vdots \\ \tilde{\mathbf{x}}_1^{(K)}(t) & \cdots & \tilde{\mathbf{x}}_d^{(K)}(t) \end{bmatrix} \quad t = t_1, \dots, t_N \quad (4)$$

where t refers to the time points, N the length of the time-series, K the number of trials and d the number of ROIs.

Then the data in $\tilde{\mathbf{X}}$ are fitted against a tvMVAR model in the general form:

$$\tilde{\mathbf{X}}(t) = -\sum_{r=1}^p \mathbf{A}_r(t) \mathbf{X}(t-r) + \mathbf{W}(t) \quad (5)$$

where $\mathbf{A}_r(t)$ are the $[d \times d]$ AR matrices containing the model coefficients, $\mathbf{W}(t)$ is the stationarity zero-mean white noise process also called innovation process with covariance matrix Σ_w , and p is the model order, usually estimated by means of the Akaike Information Criteria for MVAR processes [61]. The General Linear Kalman filter approach is applied in order to estimate the coefficients of the time-variant AR matrices and the innovation process Σ_w [62].

As the MVAR model is estimated, for each time-point t , having defined the complex matrix $\mathbf{B}(f)$ as:

$$\mathbf{B}(f) = \mathbf{I}_d - \sum_{r=1}^p \mathbf{A}_r e^{-j2\pi f r} \quad (6)$$

where \mathbf{I}_d is the identity matrix and j is the imaginary unit in this equation, the *iPDC* complex function from the time-series j to the time-series i is obtained by:

$$iPDC_{i \leftarrow j}(f) = \sigma_{w_{ii}}^{-1/2} \frac{b_{ij}(f)}{\sqrt{\mathbf{b}_j^H(f) \Sigma_w^{-1} \mathbf{b}_j(f)}} \quad (7)$$

where $\mathbf{b}_j(f)$ and $b_{ij}(f)$ are respectively the j -th column and the (j, i) -th element of matrix $\mathbf{B}(f)$, $\sigma_{w_{ii}}$ is the (i, i) -th element of the innovation covariance matrix Σ_w , and the apex H in \mathbf{b}_j^H stands for Hermitian transpose, i.e., obtained from \mathbf{b}_j by taking the transpose and then the complex conjugate of its components.

The complex function $iPDC_{i \leftarrow j}(f)$ of eq. (7) is usually analysed in terms of its absolute value.

Simulation

To test if the SVD method is capable of detecting an effective connectivity map of the human brain, we simulated a simple four-node (ROI) network with different delays. We generated the time-course of the dipoles laying in the right occipital region of the brain and then a delayed version of 3 ms with the same profile in the left occipital region. The same signals with a reduced amplitude (80%) and a delay of 5 ms were placed in the the left and right inferior temporal regions of the brain. The time-course chosen was the average VEP reconstructed in the source space of the Dataset 1 in the right occipital cortex in the first 500 ms after the stimulus. The orientation of the dipoles was chosen perpendicular to the cortex. Each realization had a sample rate of 200 Hz with 100 time points.

After having reconstructed these waveforms, white Gaussian noise with a SNR=5 was added to the simulated waveforms and it also generated the background activity of the other dipoles of the model. These $M=5000$ dipoles were then multiplied with the lead field matrix L estimated for each subject of the Dataset 1 obtaining the simulated EEG. We obtained 20 epochs for each subject by adding 20 different profiles of noise.

239 RESULTS

240 *Application on visual evoked potentials*

241 In **Figure 1** (panel (a)), we report the dipoles (arrows in the figure) representing the source waveforms in the
242 right lateral occipital cortex of a representative subject (sub #1) in the 500 ms after the face stimulus from
243 different perspective views. We chose the right lateral occipital cortex to visualize the results, because we clearly
244 localized the N170 component in this region. In addition, this source localization is also consistent with the
245 literature [63] using MRI localizer scan that revealed two additional extrastriate regions beyond the fusiform face
246 area that responded more strongly when subjects viewed faces than when they viewed objects. These include
247 brain regions in the occipital gyri and in the superior temporal sulcus [41]. To be able to compress four dimensions,
248 i.e., x, y, z and *time* axes, in a 2-D figure, the x -axis is carrying both the information of the x dimension and
249 the *time* dimension. In other words, we rigid translated each dipole along the x -dimension to represent its time
250 evolution. In panel (b), we report the three different projection planes of the space represented in panel (a). In
251 panel (c), the time-series representing the time-course of the source waveforms in the right lateral occipital cortex
252 projected in the x, y and z axes are depicted respectively from top to bottom. Interestingly, in the estimated VEP
253 source waveforms after the visual stimulus, the orientation over time of all the set of dipoles is not random.
254 Furthermore, we qualitatively observe the existence of a main direction that maximizes the magnitude of the
255 majority of dipoles. Having noticed that, summing the dipoles content in each ROI by the orthonormal vector
256 projected along the axis in space that represents the major orientation of all the dipoles should explain most the
257 variability of the data and be an accurate representation of the ROI content.

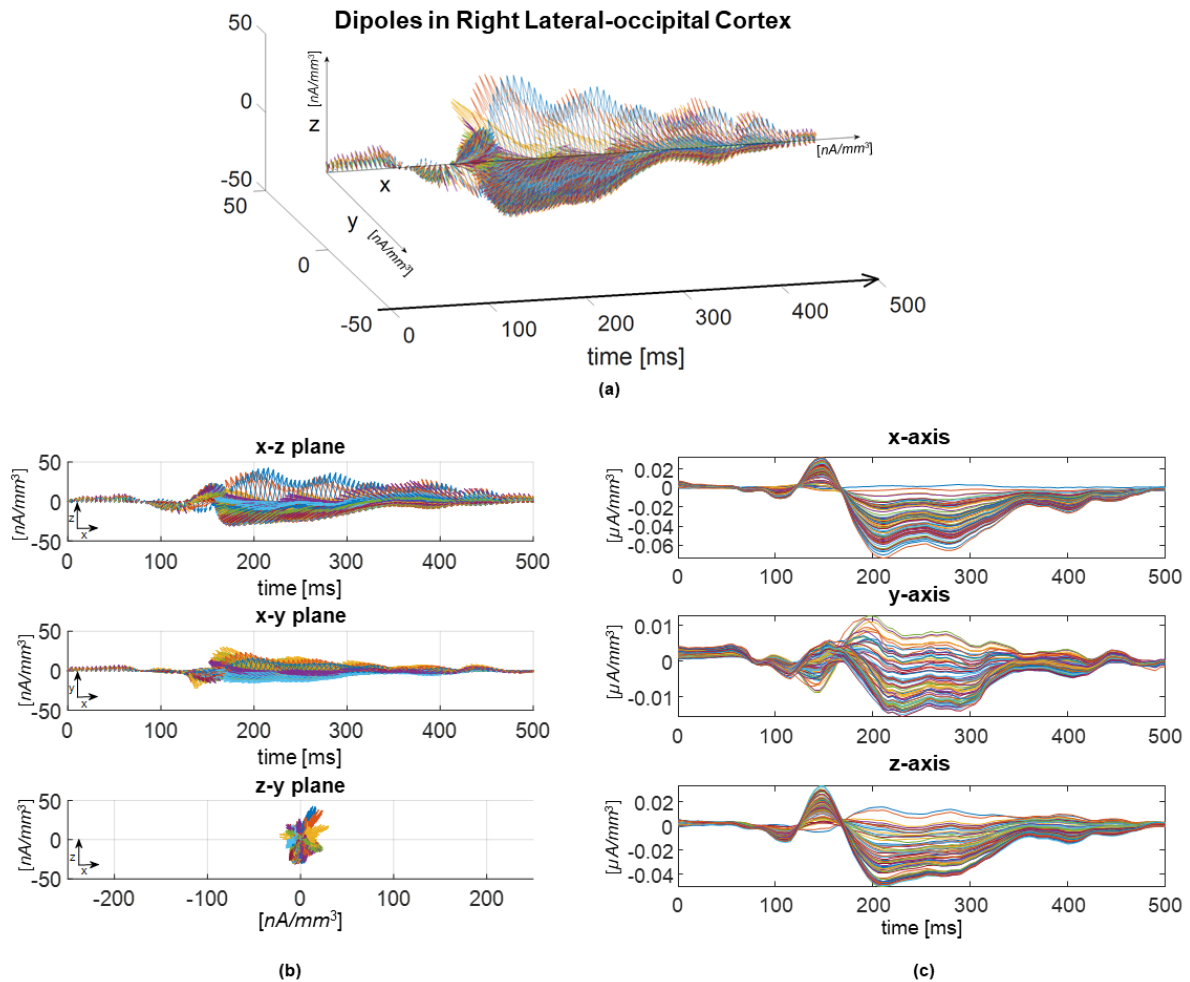


Figure 1 (a) All dipoles representing the solution points in the source space are reported as arrows. Each colour represents the dynamics of a different dipole over time in the right lateral-occipital brain region in a representative subject (sub #1). (b) Views of the x-z-plane, x-y-plane and z-y plane are represented from top to bottom for dipoles of panel (a). (c) x- y- z- time-components of all the dipoles in the Right Lateral-occipital region.

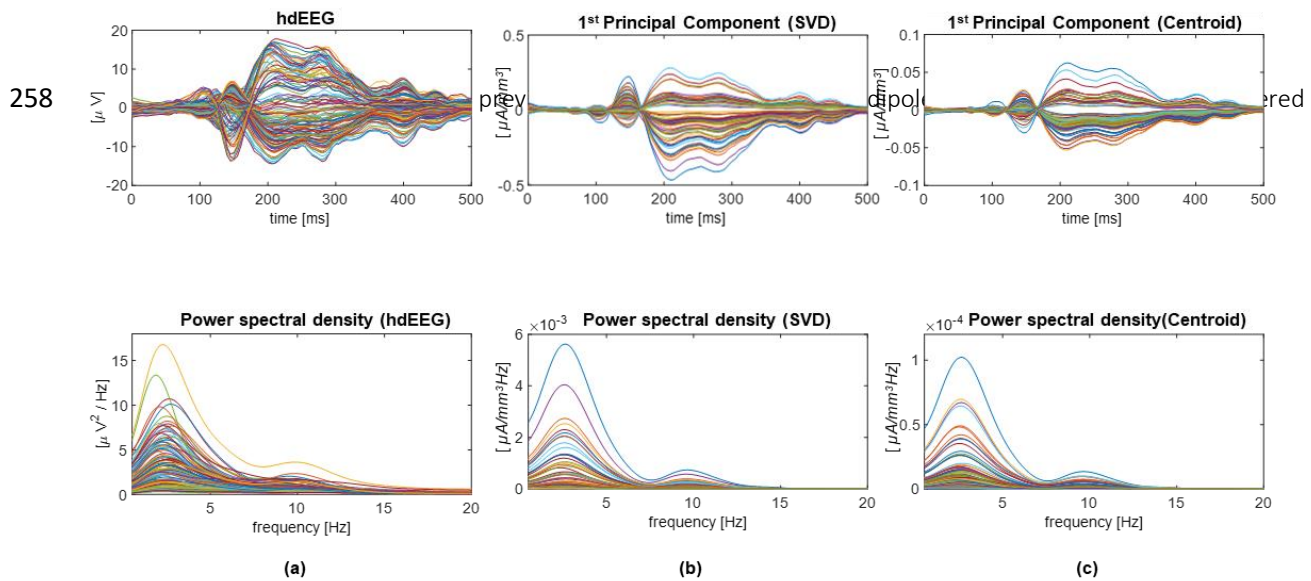
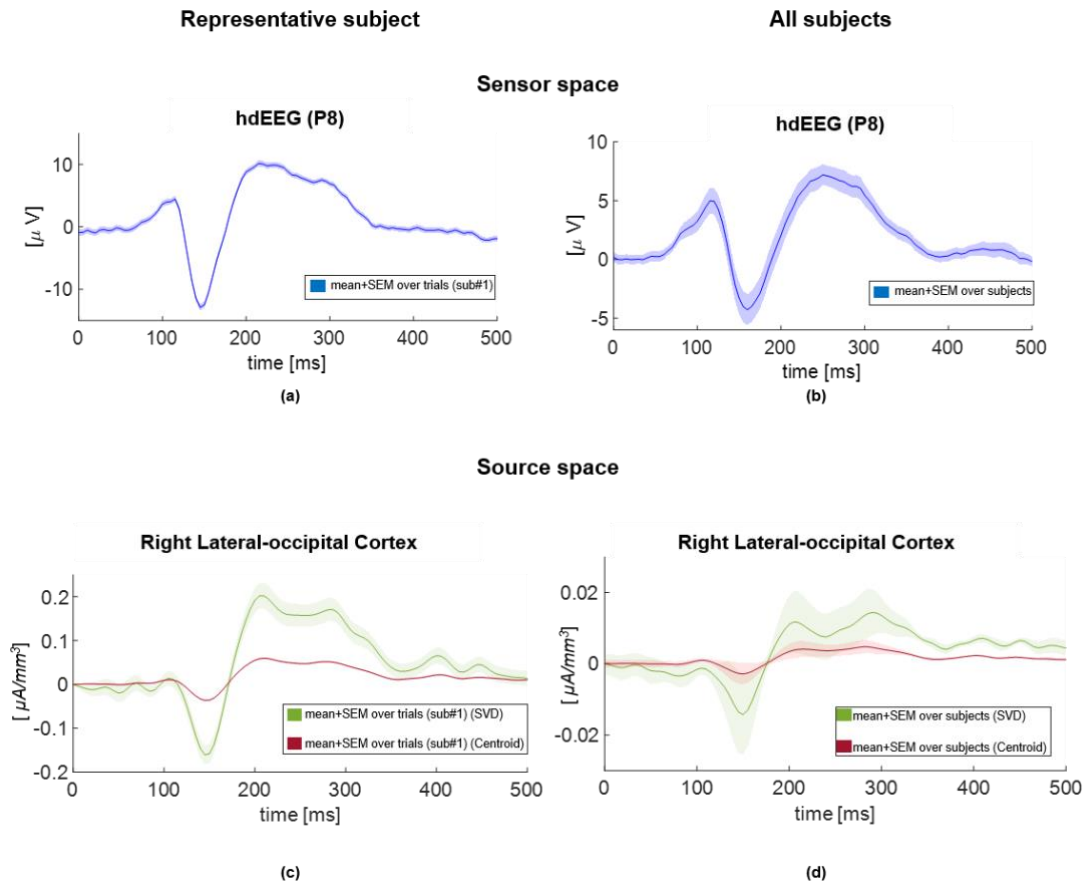


Figure 2 Signal and corresponding power spectral density average among trials of (a) 128 high-density EEG time-courses representing the visual evoked potential in a representative subject (sub #1), (b) ROI time-series computed through SVD in sub #1, and (c) the first principal component of the time-series lying in the centroid of each ROI.

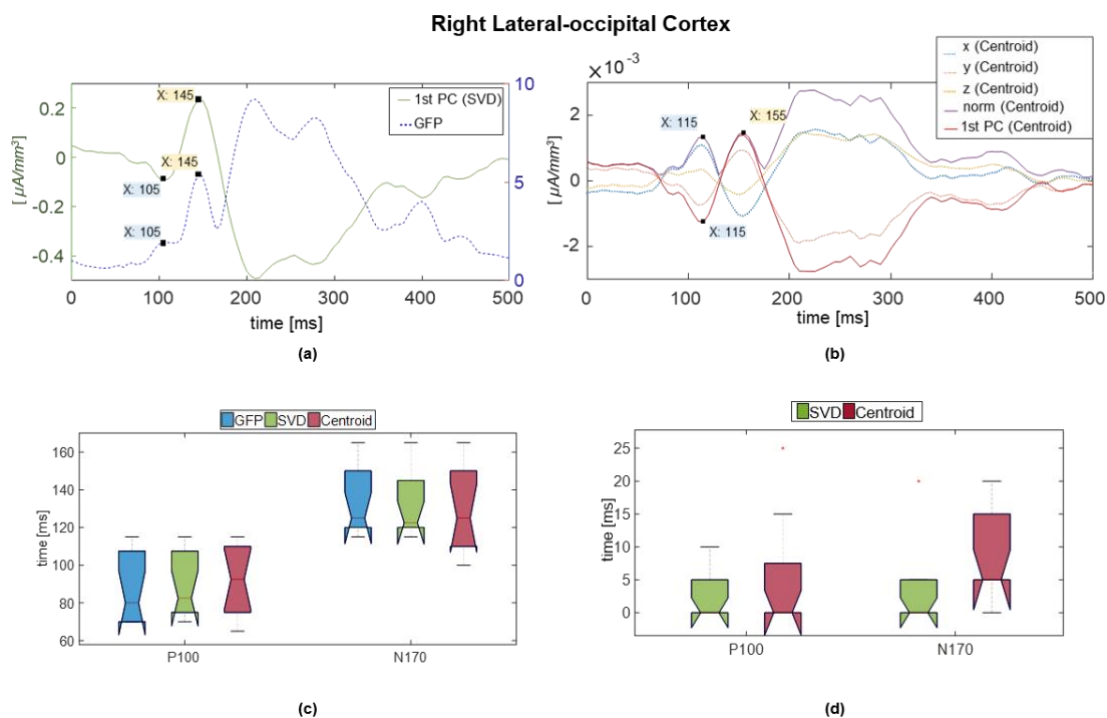
259 as representative for the entire ROI. For this reason, in **Figure 2**, we compared the temporal patterns and the
260 frequency content of the hdEEG recordings 500 ms following the stimulus presentation (panel (a)) with the
261 reconstructed time-series in the inverse space obtained from the proposed SVD method (panel (b)) and the source
262 activity in the centroid (panel (c)) for sub#1. In panels (b) and (c) respectively, we reported the first principal
263 component computed from both the first eigenvector for each ROI and for the three x- y- z- components of the
264 source activity in the centroid. After applying SVD, dealing directly with the first eigenvector or re-projecting the
265 first eigenvector on the original data space is a user choice. It depends if the user needs to deal with normalized
266 time-series or if she/he cares about the amplitude content of the signal. Observing both the proposed
267 reconstruction (**Figure 2** panel (b)) and the centroid time-series (**Figure 2** panel (c)), we found that they strongly
268 differ in the amplitude magnitude as visible in their absolute power spectral density values. However, the relative
269 power distribution among the canonical EEG-frequency bands does not significantly differ between the two
270 different reconstructions (Mann-Whitney U-test, $p>0.98$).

271 To emphasize the differences between the two methods, we compared the ability in detecting the P100 and
272 N170 peaks of the proposed representative time-series based on SVD computation and the centroid one. P100 is
273 the first dominant component in response to visual stimuli with a lateral occipital positivity [64], followed by the
274 N170. The N170 is a component of the evoked potential that reflects the neural processing of faces and its
275 response should be maximal over occipital-temporal electrodes [65] [66]. In **Figure 3**, we report for a
276 representative subject and for all the subjects the average EEG signal in the sensor space at electrode B11 (P8)
277 located over the right parietal lobe (panels (a) and (b)) and the reconstructed time-series in the source space
278 through the SVD and the centroid in the right lateral-occipital cortex (panels (c) and (d)). **Figure 3** shows that the
279 centroid time-series has lower amplitude and a flatter morphology than the SVD time-series in a representative
280 subject (panel (c)) and across subjects (panel (d)) in the source space. The results in **Figure 3** confirmed that the
281 SVD time-series present a coherent pattern compared to the signal recorded on the scalp and the amplitude and
282 the latency of the peaks of interest can be easily estimated. In order to check for latency differences between the
283 methods, we computed as reference the Global Field Power (GFP) [52] from the hdEEG for each subject in order
284 to determine the latency of the maxima of the components P100 and N170. For instance, for sub#1, the two
285 detected latencies were $t=105$ ms for P100 and $t=145$ ms for N170. We then calculated the inverse solution on
286 the average evoked potential with Cartool [52] and we localized the ROI containing the maximum of the norm of
287 the source waveforms for both peaks. We then compared the latencies estimated in the time-series obtained by
288 the proposed projection method (**Figure 4** panel (a)) with the time-series derived from the centroid method
289 (**Figure 4** panel (b)) in the selected ROI. Results in a boxplot form (**Figure 4** panel (c)) show the latencies
290 estimated through the GFP, in blue, the SVD time-series, in green, and the centroid time series, in red. **Figure 4**
291 panel (d) shows that the absolute difference between the latencies estimated through the GFP and the
292 reconstructed time-series in the source space is higher for the centroid compared to the SVD time-series. From
293 this evaluation, the SVD time-series seem to more reliably estimate the peak latencies in the VEP.



294

295 *Figure 3 . (a) Average \pm SEM among trials of the EEG signal recorded on B11 (P8) electrode in sub#1. (b) Average \pm SEM*
296 *among subjects of the average of the EEG signal on B11 (P8). (c) Average \pm SEM among trials of the proposed representative*
297 *time-series in the source space computed through SVD (green) and of the centroid (red) in sub#1 in the right lateral-occipital*
298 *cortex. (d) Average \pm SEM among subjects of the average proposed representative time-series computed through SVD (green)*
299 *and of the average centroid (red) in the right lateral-occipital cortex.*



300

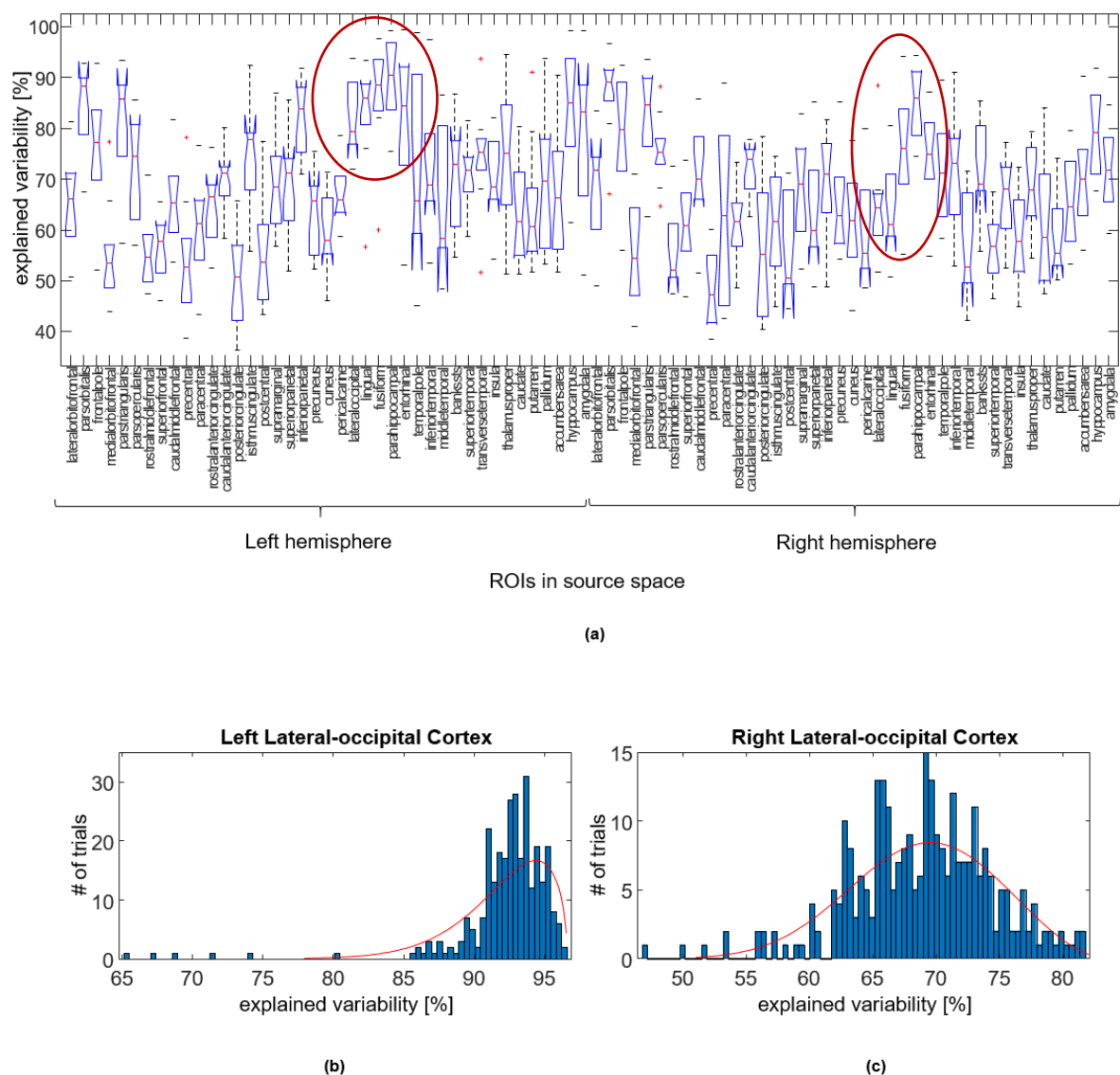
301 *Figure 4 (a) Proposed representative time-series (green) computed through SVD for the Right Lateral-occipital region. (b)*
 302 *Norm (violet) and the first principal component (green) of the x- y- z- time-components (respectively, blue, orange and yellow*
 303 *dotted lines) of the dipole lying in the centroid of the Right Lateral-occipital region. (c) Boxplot representing the latency in*
 304 *ms for each subject for P100 and N170 estimated through the EEG GFP (blue), the representative time-series computed*
 305 *through SVD (green) and the centroid time-series (red). (d) Boxplot representing the absolute difference in latency in ms for*
 306 *each subject for P100 and N170 estimated between the EEG GFP and the representative time-series computed through SVD*
 307 *(green) and the centroid time-series (red).*

308 We then computed the values of the explained variance (average among trials) of each of the 82
 309 representative time-series summing up the information content of the ROIs for all the subjects (Figure 5 panel
 310 (a)). The majority of the brain areas expected to be involved in face perception (red circles in Figure 5) show
 311 higher explained variance. In Figure 5 panels (b) and (c), we report the histogram containing all the explained
 312 variances for all the trials for sub#1 fitted against the generalized extreme value distribution [43]. For instance,
 313 the average value of the location parameter was 94% for the left lateral occipital cortex and 70% for the right
 314 lateral occipital cortex in sub#1.

315 Finally, after computing the |iPDC| values during the first 500 ms after the stimulus, we compared the values
 316 of the outflow from each ROIs at N170 among the reconstructions based on SVD, the selection of the centroid for
 317 each ROI and the selection of the time-series containing the maximum power for each ROI [27]. The connectivity
 318 patterns between the different cortical regions were summarized by representing the total outflow from a cortical
 319 region toward the others, generated by the sum of all the statistically significant links obtained by application of
 320 the iPDC to the cortical waveforms (with their values). The total outflow for each ROI is represented by a sphere
 321 centered on the cortical region, whose radius is linearly related to the magnitude of all the outgoing directed
 322 links to the other regions. Such information is also coded through a color scale. The greatest amount of
 323 information outflow depicts the ROI as one of the main sources (drivers) of functional connections to the other
 324 ROIs [67]. In Figure 6, we report the average values computed across subject of the outflow for the SVD-time-

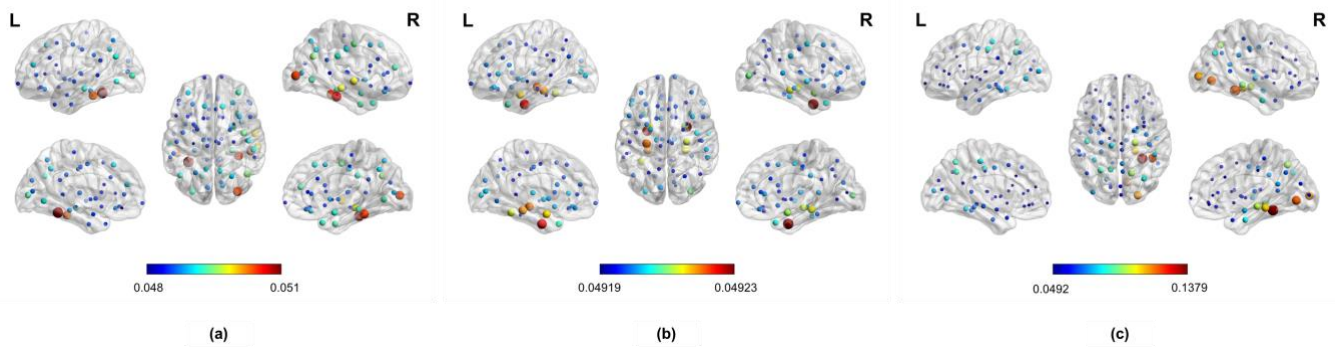
325 series, the centroid time-series and the maximum-power time-series. We can note that the ROIs with the
 326 maximum outflow (>95% percentile) were localized in the right lateral-occipital cortex, and in the inferior
 327 temporal cortex (panel (a)) when using the SVD reconstruction, in mesial temporal cortex near the hippocampus
 328 (panel (b)) when using the centroid time-series and in the right lateral-occipital cortex and in the right inferior
 329 temporal cortex (panel (c)) when using the maximum-power time-series. In the literature, the generation of N170
 330 was proposed to be attributed to neural sources in lateral, basal temporal, and extrastriate occipital cortices [63]
 331 [68] [69] [70] [71] [72], to the fusiform gyrus of the inferior temporal cortex [73] in recognition of faces, which is
 332 in accordance with our estimation through the SVD reconstruction. The SVD reconstruction results in a precise
 333 and less blurry localization of the major drivers for the proposed VEP.

334



335

336 *Figure 5. VEP: (a) Boxplot representing the percentage of explained variability for the proposed representative time-series*
 337 *for each ROI computed though SVD for all the subjects. Red circles highlight the ROIs that are mainly involved in the VEP.*
 338 *(b) Histogram representing the percentage of explained variance in the representative subject (sub #1) for all the time-series*
 339 *representing the left lateral-occipital brain region. (c) Histogram representing the percentage of explained variance in sub #1*
 340 *for all the time-series representing the right lateral-occipital brain region.*



341

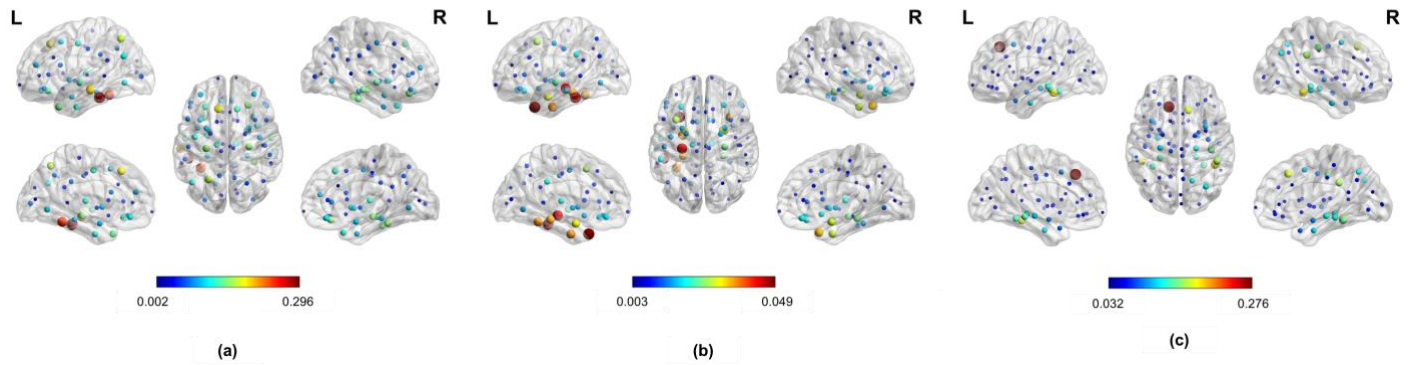
342 *Figure 6 VEP: Mean outflow across subjects computed from iPDC matrix for (a) the SVD time-series, (b) the centroid time-*
343 *series and (c) the maximum-power time-series. Nodes dimension and colour identify the value of the outflow.*

344

345 *Application on interictal spikes*

346 For each epileptic patient, we applied our method to compute the representative time-series for each ROI.
347 First, we evaluated if the frequency distribution did not significantly differ passing from the scalp EEG to our
348 inverse representation. The Mann-Whitney U-test confirmed that the relative power distributions between scalp
349 EEG and our inverse representation were not different in each frequency band for each patient ($p > 0.95$). After
350 that, in order to compare the power of localization among the SVD time-series, the centroid time-series and the
351 maximum-power time-series, we selected 7 patients with anterior-mesial temporal lobe epilepsy with ILAE class
352 I after surgery, i.e., completely seizure free, no auras [74], in which part of the left temporal lobe was removed.
353 For each patient, after computing the iPDC matrices, we estimated the outflow of information from each ROI
354 during the advent of the spike. In **Figure 7** we report the mean outflow across patients computed with the SVD-
355 time-series (panel (a)), the centroid time-series (panel (b)) and the maximum-power time-series (panel (c)). The
356 ROIs with the value of the outflow above the 95% percentile, considered to be the main drivers during the advent
357 of the spikes are: left fusiform, middle-temporal brain areas for the SVD time-series, left temporal-pole brain areas
358 near the hippocampus for the centroid time-series and left inferior frontal brain areas for the maximum-power
359 time-series. The first two methods correctly identified the left temporal lobe, but for the centroid time-series we
360 can note that the range of outflow values (colorbar in panel (b)) is almost 10 times smaller compared to the one
361 of the SVD time-series (colorbar in panel (a)), thus, the resolution obtained exploiting the SVD resulted to be
362 higher. We used the postoperative structural MRI as validation for the localization of the generators of the
363 interictal epileptic discharges, the area removed from the surgery was the left anterior temporal lobe for all the
364 7 patients classified as good outcome. Moreover, considering all the patients, we computed the laterality index
365 defined as in [32] to assess whether this group of patients had more summed outflow ipsilateral or contralateral
366 to the epileptic source. We found that 7 out of 7 patients had a greater ipsilateral outflow exploiting the SVD time-
367 series, whereas 4 out of 7 exploiting the centroid time-series. In addition, we computed the mean efficiency of
368 the network across patients. Efficiency is a measure of how efficiently each node exchanges information. Using
369 the SVD time-series we found that the most efficient nodes of the network (with values above the 95% percentile)

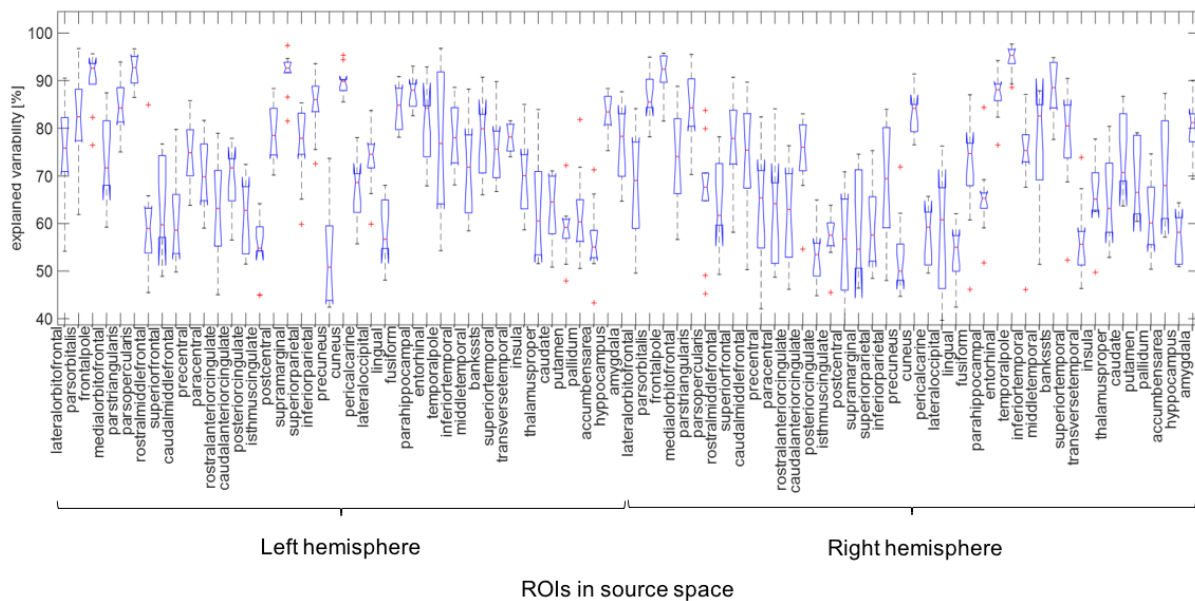
370 were the left fusiform and the left middle-temporal brain areas, the same brain areas labeled as main drivers by
371 the outflow measure. Brain regions having high efficiency suggest the existence of a high level of efficiency in
372 communicating with the rest of the brain during the advent of the spike [75].



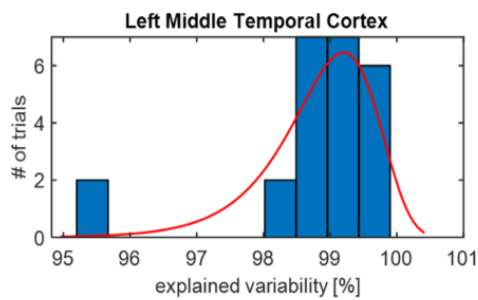
373

374 *Figure 7 Interictal spikes: Mean outflow across good-outcome patients with left temporal lobe epilepsy computed from iPDC*
375 *matrix for (a) the SVD time-series, (b) the centroid time-series and (c) the maximum-power time-series. Nodes dimension and*
376 *color identify the value of the outflow.*

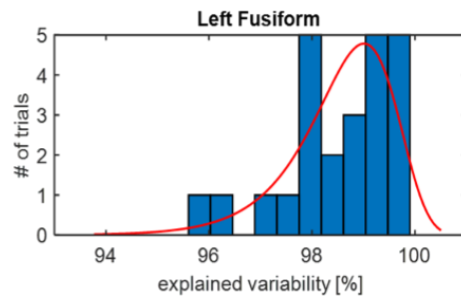
377 Finally, we computed the values of the explained variance of each of the 82 representative time-series
 378 summing up the information content of the ROIs in all the trials/epochs for each subject (Figure 8). Each obtained
 379 histogram was fitted against the generalized extreme value distribution [76]. The average value of the location
 380 parameter \pm scale parameter was $75\% \pm 15\%$. Considering that we are trying to summarize the content of three
 381 different time-series in a unique signal, explaining more than 60% of the variance of all the dipoles in a ROI means
 382 being able to capture and describe at least the information contained in two out of three components. The data



(a)



(b)



(c)

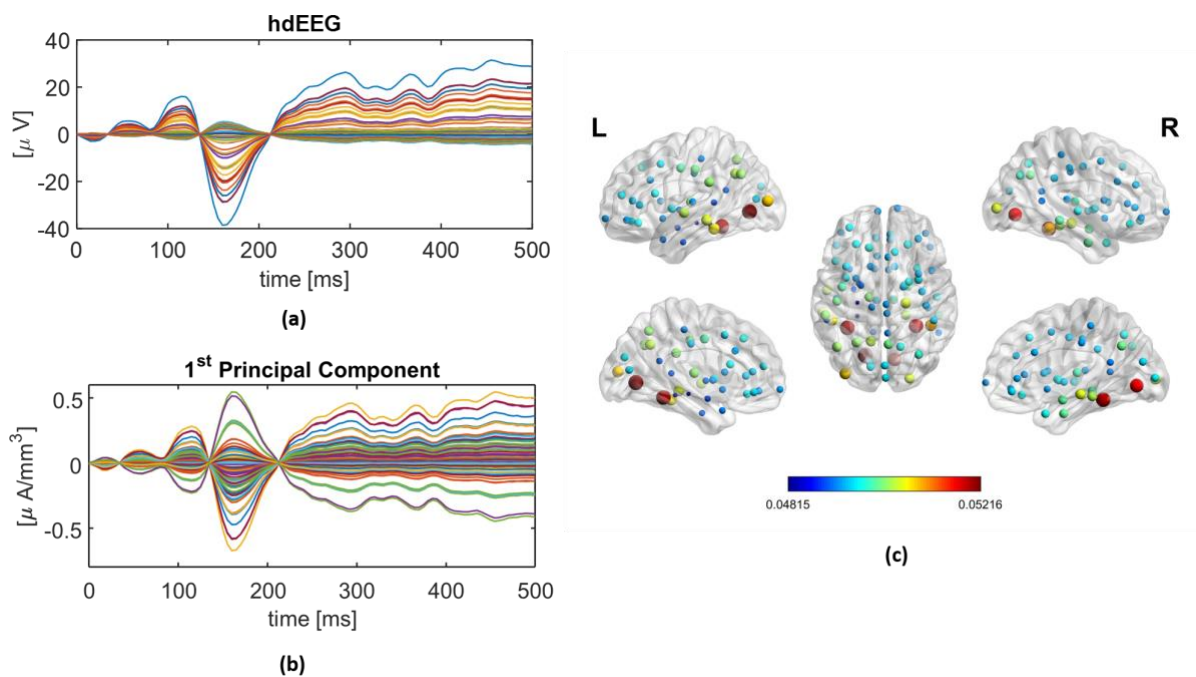
Figure 8 Interictal spikes: Boxplot representing the percentage of explained variability for the proposed representative time-series for each ROI computed though SVD for all the subjects. (b) Histogram representing the percentage of explained variance in the representative subject (sub #1) for all the time-series representing the left middle temporal cortex. (c) Histogram representing the percentage of explained variance in sub #1 for all the time-series representing the left fusiform brain region.

383 loss in a dimensionality reduction is unavoidable, but the fraction of the variance of the original data explained
384 with our one-dimension representation seems to be a good achievement.

385

386 *Application on simulated data*

387 In Figure 9 (panel (a)), the simulated 128 hdEEG time-courses averaged among the 20 trials for one of the 13
388 simulated subjects are shown. These hdEEG signals were the input of the LAURA algorithm to estimate the source
389 waveforms. The obtained SVD time-series averaged among the 20 trials for the same simulated subject of panel
390 (a) are reported in panel (b). After computing the $|iPDC|$ values during the first 500 ms after the stimulus, we
391 compared the values of the outflow from each ROIs at N170 for all the simulated subjects. The ROIs with the
392 maximum outflow (>95% percentile) were consistently localized in the right lateral-occipital cortex, and in the
393 inferior temporal cortex as imposed by the simulation. The average outflow across all simulated subjects is
394 displayed in Figure 9 (panel (c)).



395

396 *Figure 9 Simulated VEP: (a) 128 high-density EEG time-courses and (b) ROI time-series computed through SVD average*
397 *among trials in a representative simulated subject, and (c) mean outflow across all simulated subjects computed from iPDC*
398 *matrix for the SVD time-series. Nodes dimension and colour identify the value of the outflow.*

399 CONCLUSION AND DISCUSSION

400 With the final aim to improve connectivity estimation, we proposed a method able to overcome both the
401 dipole orientation problem and to sum up of the information of different solution points in the same region of
402 interest. The proposed projection method based on singular value decomposition sums up the information carried
403 by hundreds of 3-D time-series in a unique 1-D signal representing most of the variability of the sources in each
404 region of interest. Thanks to the orthogonality constraints (UV are orthogonal matrices and S is a diagonal matrix),
405 the solution of SVD is unique and can be considered a reliable way for dimensionality reduction. The amplitude
406 of the representative signal computed as the first orthonormal vector of the unitary matrix U is by definition
407 independent on the original signal amplitudes. Thus, this solution overcomes a major drawback of the common

408 procedure of averaging the dipoles, namely drastically reduced amplitudes after averaging all the dipoles in the
409 same region of interest. Dealing with smaller amplitudes may distort the results of the connectivity estimation
410 because it involves computing of the inverse of the matrix containing the data [20] [77].

411 Additionally, we proposed a method able to create a *population* signal that summarizes the sources activity in
412 each region of interest (ROI) giving an indication of the global explained variance and considering all gray matter
413 solution points in the brain. In the majority of previous studies, a few voxels are selected for each ROI, for example
414 the most active voxels, and afterwards the information carried by these most active voxels is summarized in a
415 unique signal by a decomposition method. Indeed, in [29] [30], the authors defined the ROIs by carefully selecting
416 voxels corresponding to cortical areas that showed significant differences in the gamma-band range. For analyzing
417 the information transfer between the identified regions of interest in source space through partial-directed-
418 coherence, a multivariate autoregressive model was fitted to the time series revealed by the inverse solution at
419 each ROI. To overcome the problem that each current source density consists of three directions (X, Y and Z), they
420 computed the first principal component of each triplet. In our work, we aimed to create a population signal
421 directly from the activity of all the voxels contained in the same ROI without introducing a priori condition to
422 select specific points/areas. Also in [38], an fMRI connectivity analysis approach combining both principal
423 component analysis (PCA) and Granger causality method was proposed to study directional influence between
424 functional brain regions, but before applying this combined measure, the authors selected only the activated
425 brain regions/voxels with BrainVoyager QX.

426 Moreover, the computational cost should also be considered as it influences the usefulness of the method in
427 practice. The computational cost of singular value decomposition is much lower than the computational cost of
428 other approaches based on the canonical polyadic decomposition [78]. We also showed that the projection
429 method based on SVD provides robust results for visual evoked potentials and epileptic spikes. The results have
430 also been confirmed by simulations. Furthermore, by analysing the frequency content of the proposed time-series
431 and comparing its features with the centroid time-series, the signal based on the SVD seemed to both resemble
432 the EEG scalp observations features and to prevent to deal with signals with too low amplitudes for the
433 subsequent connectivity estimation. The novelty of the SVD method also lies in the fact that it exploits the
434 information of the overall population of dipoles in each ROI instead of considering only one time-series as
435 representative of the complex activity pattern in a given brain region. Despite the lack of availability of an objective
436 ground truth in both estimating the source activities and the causal interactions among them, observing the
437 dynamics and the orientation of the dipoles over time in visual evoked potential and epileptic spikes seems to
438 confirm the existence of a principal component that accounts for most of the variability in the data.

439 Since the results may be influenced by the choice of the algorithm for estimating the source waveforms and
440 from the brain parcellation, there are other approaches to define EEG networks that circumvent the issue of how
441 to best segment the source maps into ROIs [79] by explaining the EEG in terms of a discrete set of causally
442 interacting clusters. However, this direct approach relies on several assumptions such as (1) bioelectromagnetic
443 activity is generated by a set of distributed sources; (2) the dynamics of these sources can be modelled as random

444 fluctuations of a small number of mesostates; (3) the number of mesostates engaged by a cognitive task is small;
445 (4) the mesostates interact according to a full Dynamical Causal Network that can be estimated; (5) the dynamics
446 of the mesostates can switch between multiple approximately linear operating regimes; (6) each operating regime
447 remains stable over finite periods of time (temporal clusters); and (7) the total number of times the mesostates'
448 dynamics can switch is small. Our intention was to estimate source activity in the whole brain without any a priori
449 assumption about the number and distribution of the sources. Such an approach is better suited in studies that
450 aim to compare and combine the effective connectivity among ROIs with the structural connectivity estimated by
451 diffusion MRI in the same framework.

452 FUNDING: This study was supported by the Swiss National Science Foundation (Grant No. CRSII5-170873 to PH, PvM, GP, SV and CMM;
453 Grant No. 320030_159705 to CMM; Grant No. PP00P1_157420 to GP; No. 320030-169198 to SV), by the National Centre of Competence in
454 Research (NCCR) "SYNAPSY—The Synaptic Basis of Mental Diseases" (NCCR Synapsy Grant No. 51NF40-158776 to PH and CMM), by the
455 Foundation Gertrude Von Meissner (to SV), and by the European Union's Horizon 2020 research and innovation program under the Marie
456 Skłodowska-Curie grant agreement (Grant No. 660230 to PvM).

457 CONFLICT OF INTEREST: The authors declare they have no conflict of interest.

458 REFERENCES 459

- [1] J. C. De Munck, B. W. Van Dijk and H. E. N. K. Spekreijse, "Mathematical dipoles are adequate to describe realistic generators of human brain activity," *IEEE Transactions on Biomedical Engineering*, vol. 35, no. 11, pp. 960-966, 1988.
- [2] F. Van de Steen, L. Faes, E. Karahan, J. Songriri, P. A. Valdes-Sosa and D. Marinazzo, "Critical comments on EEG sensor space dynamical connectivity analysis," *Brain topography*, pp. 1-12, 2016.
- [3] S. Haufe, V. V. Nikulin, K. R. Muller and G. Nolte, "A critical assessment of connectivity measures for EEG data: a simulation study," *Neuroimage*, vol. 64, pp. 120-133, 2013.
- [4] C. Brunner, M. Billinger, M. Seeber, T. R. Mullen and S. Makeig, "Volume conduction influences scalp-based connectivity estimates," *Frontiers in computational neuroscience*, vol. 10, p. 121, 2016.
- [5] C. M. Michel and B. He, "EEG Mapping and Source Imaging," in *Niedermeyer's Electroencephalography: Basic Principles, Clinical Applications, and Related Fields*, Seventh Edition ed., New York, Oxford University Press, 2018, pp. 1135-1156.
- [6] C. M. Michel, M. M. Murray, G. Lantz, S. Gonzales, L. Spinelli and R. G. De Peralta, "EEG source imaging," *Clinical Neurophysiology*, vol. 115, no. 10, pp. 2195-2222, 2004.
- [7] C. M. Michel and M. M. Murray, "Towards the utilization of EEG as a brain imaging tool," *Neuroimage*, vol. 61, no. 2, pp. 371-385, 2012.
- [8] C. M. Michel and B. He, "EEG mapping and source imaging.," in *Niedermeyer's Electroencephalography: Basic Principles, Clinical Applications, and Related Fields: Sixth Edition*, Wolters Kluwer Health Adis (ESP), 2012, pp. 1179-1202.
- [9] R. Grech, T. Cassar, J. Muscat, K. P. Camilleri, S. G. Fabri, M. Zervakis, P. Xanthopoulos, V. Sakkalis and B. Vanrumste, "Review on solving the inverse problem in EEG source analysis," *Journal of neuroengineering and rehabilitation*, vol. 7:5, no. 1, p. 25, 2008.
- [10] R. G. De Peralta Menendez, M. M. Murray, C. M. Michel, R. Martuzzi and S. L. Gonzalez-Andino, "Electrical neuroimaging based on biophysical constraints," *Neuroimage*, vol. 21, no. 2, pp. 527-539, 2004.
- [11] M. A. de Reus and M. P. Van den Heuvel, "The parcellation-based connectome: limitations and extensions," *Neuroimage*, vol. 80, pp. 397-404, 2013.
- [12] N. Tzourio-Mazoyer, "Automated anatomical labeling of activations in SPM using a macroscopic anatomical parcellation of the MNI mRI single-subject brain," *NeuroImage*, vol. 15, pp. 273-289, 2002.

- [13] A. C. Evans, A. L. Janke, D. L. Collins and S. Baillet, "Brain templates and atlases," *NeuroImage*, vol. 62, no. 2, pp. 911-922, 2012.
- [14] R. Desikan, F. Ségonne, B. Fischl, B. Quinn, B. Dickerson, D. Blacker, R. Buckner, A. Dale, R.-P. Maguire, B. Hyman, M. Albert and R. Killiany, "An automated labeling system for subdividing the human cerebral cortex on MRI scans into gyral based regions of interest," *Neuroimage*, vol. 31, no. 3, pp. 968-980, 2006.
- [15] B. Fischl, A. Van Der Kouwe, C. Destrieux, E. Halgren, F. Ségonne, D. H. Salat, E. Busa, L. J. Seidman, J. Goldstein, D. V. Caviness, N. Makris, B. Rosen and A. M. Dale, "Automatically parcellating the human cerebral cortex," *Cerebral cortex*, vol. 14, no. 1, pp. 11-22, 2004.
- [16] M. Rubinov and O. Sporns, "Complex network measures of brain connectivity: uses and interpretations," *NeuroImage*, vol. 52, no. 3, pp. 1059-1069, 2010.
- [17] G. Nolte, O. Bai, L. Wheaton, Z. Mari, S. Vorbach and M. Hallet, "Identifying true brain interaction from EEG data using imaginary part of coherency," *Clinical Neurophysiology*, vol. 115, no. 10, pp. 2292-2307, 2004.
- [18] C. J. Stam, G. Nolte and A. Daffertshofer, "Phase lagg index: assessment of functional connectivity from multi channel EEG and MEG with diminished bias from common sources," *Human brain mapping*, vol. 28, no. 11, pp. 1178-1193, 2007.
- [19] A. A. Ioannides, L. C. Liu, J. Kwapien, S. Drozd and M. Streit, "Coupling of regional activations in a human brain during an object and face affect recognition task," *Human brain mapping*, vol. 11, pp. 77-92, 2000.
- [20] L. A. Baccalà and S. Koichi, "Partial directed coherence," in *Methods in brain connectivity inference through multivariate time series analysis*, CRC Press, 2014, pp. 57-73.
- [21] M. Wibral, R. Vicente and M. Lindner, "Transfer entropy in neuroscience," in *Directed information measures in neuroscience*, Berlin Heidelberg, Springer, 2014, pp. 3-36.
- [22] A. P. Baker, M. J. Brookes, I. A. Rezek, S. M. Smith, T. Behrens, P. J. Probert Smith and M. Woolrich, "Fast transient networks in spontaneous human brain activity," *Elife*, vol. 3, pp. 1-18, 2014.
- [23] M. J. Brookes, M. Woolrich, H. Luckhoo, D. Price, J. R. Hale, M. C. Stephenson, G. R. Barnes, S. M. Smith and P. G. Morris, "Investigating the electrophysiological basis of resting state networks using magnetoencephalography," *PNAS*, vol. 108, pp. 16783-16788, 2011.
- [24] D. Vidaurre, A. J. Quinn, A. P. Baker, D. Dupret, A. Tejero-Cantero and M. W. Woolrich, "Spectrally resolved fast transient brain states in electrophysiological data," *Neuroimage*, vol. 126, pp. 81-95, 2016.
- [25] A. Coito, C. M. Michel, P. van Mierlo, S. Vulliemoz and G. Plomp, "Directed functional brain connectivity based on EEG source imaging: methodology and application to temporal lobe epilepsy," *IEEE Transactions on Biomedical Engineering*, vol. 63, no. 12, pp. 2619-2628, 2016.
- [26] C. Phillips, M. D. Rugg and K. J. Friston, "Anatomically informed basis functions for EEG source localization: combining functional and anatomical constraints," *NeuroImage*, vol. 16, no. 3, pp. 678-695, 2002.
- [27] G. R. Barnes, A. Hillebrand, I. P. Fawcett and K. D. Singh, "Realistic spatial sampling for MEG beamformer images," *Human Brain Mapping*, vol. 23, pp. 120-127, 2004.
- [28] M. Hassan, I. Merlet, A. Mheich, A. Kabbara, A. Biraben, A. Nica and F. Wendling, "Identification of interictal epileptic networks from dense-EEG," *Brain topography*, vol. 30, no. 1, pp. 60-76, 2017.
- [29] G. G. Supp, A. Schlögl, N. J. Trujillo-Barreto, M. M. Müller and T. Gruber, "Directed cortical information flow during human object recognition: analyzing induced EEG gamma-band responses in brain's source space," *PLoS One*, vol. 2, p. e684, 2007.
- [30] T. Gruber, B. Maess, N. J. Trujillo-Barreto and M. M. Müller, "Sources of synchronized induced Gamma-Band responses during a simple object recognition task: a replication study in human MEG," *Brain Research*, vol. 1196, pp. 74-84, 2008.
- [31] L. Astolfi, F. Cincotti, D. Mattia, M. G. Marciani, L. A. Baccala, F. de Vico Fallani, S. Salinari, M. Ursino, M. Zagaglia, L. Ding and J. C. Edgar, "Comparison of different cortical connectivity estimators for high-resolution EEG recordings," *Human brain mapping*, vol. 28, no. 2, pp. 143-157, 2007.
- [32] A. Coito, G. Plomp, M. Genetti, E. Abela, R. Wiest, M. Seek, C. M. Michel and S. Vulliemoz, "Dynamic directed interictal connectivity in left and right temporal lobe epilepsy," *Epilepsia*, vol. 56, no. 2, p. 207/217, 2015.

- [33] H. F. Sperdin, A. Coito, N. Kojovic, T. A. Rihs, R. K. Jan, M. Franchini, G. Plomp, S. Vulliemoz, S. Eliez, C. M. Michel and M. Schaer, "Early alterations of social brain networks in young children with autism," *eLife*, vol. 7, p. e31670, 2018.
- [34] L. Canuet, R. Ishii, R. D. Pascual-Marqui, M. Iwase, R. Kurimoto, Y. Aoki, S. Ikeda, H. Takahashi, T. Nakahachi and M. Takeda, "Resting-State EEG Source Localization and Functional Connectivity in Schizophrenia-Like Psychosis of Epilepsy," *Plos One*, vol. 6, no. 11, p. e27863, 2011.
- [35] A. Adebimpe, A. Aarabi, E. Bourel-Ponchel, M. Mahmoudzadeh and F. Wallois, "EEG Resting State Functional Connectivity Analysis in Children with Benign Epilepsy with Centrottemporal Spikes," *Front. Neurosci*, vol. 10, p. 143, 2016.
- [36] A. K. Cline, C. B. Moler, G. W. Stewart and J. H. Wilkinson, "An estimate of the condition number of a matrix," *SIAM Journal on Numerical Analysis*, vol. 16, no. 2, pp. 368-375, 1979.
- [37] P. van Mierlo, O. Lie, W. Staljanssens, A. Coito and S. Vulliemoz, "Influence of Time-Series Normalization, Number of Nodes, Connectivity and Graph Measure Selection on Seizure-Onset Zone Localization from Intracranial EEG," *Brain Topography*, pp. 1-14, 2018.
- [38] Z. Zhou, M. Ding, Y. Chen, P. Wright, Z. Lu and Y. Liu, "Detecting directional influence in fMRI connectivity analysis using PCA based Granger causality," *Brain Research*, vol. 1289, pp. 22-29, 2009.
- [39] J. V. Haxby, E. A. Hoffman and M. I. Gobbini, "The distributed human system for face perception," *Trends in cognitive sciences*, vol. 4, no. 6, pp. 223-233, 2000.
- [40] J. V. Haxby, L. G. Ungerleider, V. P. Clark, J. L. Schouten, E. A. Hoffman and A. Martin, "The effect of face inversion on activity in human neural systems for face and object perception," *Neuron*, vol. 22, no. 1, pp. 189-199, 1999.
- [41] E. Hoffman and J. Haxby, "Distinct representations of eye gaze and identity in the distributed human neural system for face perception," *Nature Neuroscience*, vol. 10, no. 3, pp. 80-84, 2000.
- [42] B. Rossion and S. Caharel, "ERP evidence for the speed of face categorization in the human brain: Disentangling the contribution of low-level visual cues from face perception," *Vision research*, vol. 51, pp. 1297-1311, 2011.
- [43] S. Bentin, T. Allison, A. Puce, E. Perez and G. McCarthy, "Electrophysiological studies of face perception in humans," *Journal of cognitive neuroscience*, vol. 8, no. 6, pp. 551-565, 1996.
- [44] J. M. Ales, F. Farzin, B. Rossion and A. M. Norcia, "Ales, J. M., Farzin, F., Rossion, B., & Norcia, A. M. (2012). An objective method for measuring face detection thresholds using the sweep steady-state visual evoked response," *Journal of vision*, vol. 12, no. 10, pp. 18-18, 2012.
- [45] V. Brodbeck, L. Spinelli, A. M. Lascano, M. Wissmeier, M. I. Vargas, S. Vulliemoz, C. Pollo, K. Schaller, C. M. Michel and M. Seeck, "Electroencephalographic source imaging: a prospective study of 152 operated epileptic patients," *Brain*, vol. 134, no. 10, pp. 2887-2897, 2011.
- [46] L. Sheybani, G. Birot, A. Contestabile, M. Seeck, J. Kiss, K. Schaller, C. M. Michel and C. Quairiaux, "Electrophysiological evidence for the development of a self-sustained large-scale epileptic network in the kainate mouse-model of temporal lobe epilepsy," *Journal of Neuroscience*, vol. 38, no. 15, pp. 3776-3791, 2018.
- [47] E. Van Diessen, W. J. E. M. Zwiiphenning, F. E. Jansen, C. J. Stam, K. P. J. Braun and W. M. Otte, "Brain network organization in focal epilepsy: a systematic review and meta-analysis," *PLOS One*, vol. 9, no. 12, 2014.
- [48] J. Engel, P. M. Thompson, J. M. Stern, R. J. Staba, A. Bragin and I. Mody, "Connectomics and epilepsy," *Current Opinion in Neurology*, vol. 26, no. 2, pp. 186-194, 2013.
- [49] M. P. Richardson, "Large brain models of epilepsy: dynamics meets connectomics," *Journal of Neurology Neurosurgery and Psychiatry*, vol. 83, no. 12, pp. 1238-1248, 2012.
- [50] N. Bigdely-Shamlo, T. Mullen, C. Kothe, K. M. Su and K. A. Robbins, "The PREP pipeline: standardized preprocessing for large-scale EEG analysis," *Frontiers in neuroinformatics*, vol. 9, no. 16, 2015.
- [51] "the Cartool Community group," [Online]. Available: cartoolcommunity.unige.ch.
- [52] D. Brunet, M. M. Murray and C. M. Michel, "Spatiotemporal analysis of multichannels EEG: CARTOOL," *Computational intelligence and neuroscience*, vol. 2011, pp. 2-15, 2011.

- [53] L. Spinelli, S. G. Andino, G. Lantz, M. Seek and C. M. Michel, "Electromagnetic inverse solution in anatomically constrained spherical head models," *Brain topography*, vol. 13, no. 2, pp. 115-125, 2000.
- [54] A. Daducci, S. Gerhard, A. Griffa, A. Lemkaddem, L. Cammoun, X. Gigandet, R. Meuli, P. Hagmann and J.-P. Thiran, "The connectome mapper: an open-source processing pipeline to map connectomes with MRI," *PLoS one*, vol. 7, no. 12, p. e48121, 2012.
- [55] "FreeSurfer Software Suite," [Online]. Available: <http://surfer.nmr.mgh.harvard.edu/>.
- [56] C. Destrieux, B. Fischl, A. Dale and E. Halgren, "Automatic parcellation of human cortical gyri and sulci using standard anatomical nomenclature," *Neuroimage*, vol. 53, no. 1, pp. 1-15, 2010.
- [57] P. C. Hansen, "Analysis of discrete ill-posed problems by means of the L-curve," *SIAM Rev*, vol. 34, pp. 561-580, 1992.
- [58] A. Cichocki, D. Mandic, L. De Lathauwer, G. Zhou, Q. Zhao, C. Caiafa and H. A. Phan, "Tensor decomposition for signal processing applications: From two-way to multiway component analysis," *IEEE Signal Processing Magazine*, vol. 32, no. 2, pp. 145-163, 2015.
- [59] K. Sameshima and L. A. Baccala, *Methods in brain connectivity inference through multivariate time series analysis*, CRC Press, 2014.
- [60] D. Y. Takahashi, L. A. Baccala and K. Sameshima, "Information partial directed coherence," *Biological cybernetics*, vol. 103, pp. 463-469, 2010.
- [61] H. Akaike, "Information theory and an extension of the maximal likelihood principle," in *Selected Papers of Hirotugu Akaike*, Springer Series in Statistics, 1998, pp. 199-213.
- [62] T. Milde, L. Leistritz, L. Astolfi, H. R. Miltner, T. Weiss, F. Babiloni and H. Witte, "A new Kalman filter approach for the estimation of high-dimensional time-variant multivariate AR models and its application in analysis of laser-evoked brain potentials," *NeuroImage*, vol. 50, pp. 960-969, 2010.
- [63] K. Grill-Spector, N. Knouf and N. Kanwisher, "The fusiform face area subserves face perception, not generic within-category identification," *Nature Neuroscience*, vol. 7, pp. 555-562, 2004.
- [64] E. Alonso Prieto, S. Caharel, R. N. Henson and B. Rossion, "Alonso Prieto, E., Caharel, S., Henson, R. N., & Rossion, B. (2011). Early (N170/M170) face-sensitivity despite right lateral occipital brain damage in acquired prosopagnosia," *Frontiers in Human Neuroscience*, vol. 5, no. 138, pp. 1-23, 2011.
- [65] A. S. Ghuman, N. M. Brunet, Y. Li, R. O. Konecky, J. A. Pyles, S. A. Walls, V. Destefino, W. Wang and M. Richardson, "Dynamic encoding of face information in the human fusiform gyrus," *Nature communications*, vol. 5, p. 5672, 2014.
- [66] B. Rossion and C. Jacques, "Does physical interstimulus variance account for early electrophysiological face sensitive responses in the human brain? Ten lessons on the N170," *Neuroimage*, vol. 39, no. 4, pp. 1959-79, 2008.
- [67] F. Babiloni, F. Cincotti, C. Carducci, C. Babiloni, F. Carducci, D. Mattia, L. Astolfi, A. Basilisco, P. M. Rossini, L. Ding, Y. Ni, J. Cheng, K. Christine, J. Sweeney and B. He, "Estimation of the cortical functional connectivity with the multimodal integration of high-resolution EEG and fMRI data by directed transfer function," *Neuroimage*, vol. 24, no. 1, pp. 118-131, 2005.
- [68] S. Bentin, T. Allison, A. Puce, E. Perez and G. McCarthy, "Electrophysiological studies of face perception in humans," *Journal of Cognitive Neuroscience*, vol. 8, no. 6, pp. 551-565, 1996.
- [69] K. A. Dalrymple, I. Oruc, B. Duchaine, R. Pancaroglu, C. J. Fox, G. Iaria, T. C. Handy and J. J. Barton, "The anatomic basis of the right face-selective N170 IN acquired prosopagnosia: a combined ERP/fMRI study," *Neuropsychologia*, vol. 49, no. 9, pp. 2553-2563, 2011.
- [70] R. J. Itier and M. J. Taylor, "N170 or N1? Spatiotemporal differences between object and face processing using ERPs," *Cerebral Cortex*, vol. 14, no. 2, pp. 132-142, 2004.
- [71] K. Botzel, S. Schulze and S. Stodieck, "Scalp topography and analysis of intracranial sources of face-evoked potentials," *Experimental brain research*, vol. 104, no. 1, pp. 135-143, 1995.
- [72] S. R. Schweinberger, E. C. Pickering, I. Jentsch, A. Burton and J. M. Kaufmann, "Event-related brain potential evidence for a response of inferior temporal cortex to familiar face repetitions," *Cognitive Brain Research*, vol. 14, no. 3, pp. 398-409, 2002.
- [73] J. D. Kropotov, "Sensory Systems and Attention Modulation," in *Functional neuromarkers for psychiatry: Applications for diagnosis and treatment*, Academic Press, 2016, pp. 137-169.

- [74] M. J. Brodie, S. M. Zuberi, I. E. Scheffer and R. S. Fisher, "The 2017 ILAE classification of seizure types and the epilepsies: what do people with epilepsy and their caregivers need to know?," *Epileptic disorders*, 2018.
- [75] T. Uehara, T. Yamasaki, T. Okamoto, T. Koike, S. Kan, S. Miyauchi, J. Kira and S. Tobimatsu, "Efficiency of a "small-world" brain network depends on consciousness level: a resting-state fMRI study," *Cerebral Cortex*, vol. 24, no. 6, pp. 1529-1539, 2013.
- [76] D. McFadden, "Modeling the choice of residential location," *Transportation Research Record*, vol. 673, 1978.
- [77] N. Moraca, "Bounds for norms of the matrix inverse and the smallest singular value," *Linear Algebra and its Applications*, vol. 429, no. 10, pp. 2589-2601, 2008.
- [78] F. Cong, Q. H. Lin, L. D. Kuang, X. F. Gong, P. Astinkainen and T. Ristaniemi, "Tensor decomposition of EEG signals: a brief review," *Journal of neuroscience methods*, vol. 248, pp. 59-69, 2015.
- [79] I. Olier, N. J. Trujillo-Barreto and W. El-Deredey, "A switching multi-scale dynamical network model of EEG/MEG.," *Neuroimage*, vol. 83, pp. 262-287, 2013.

460

461